1-1-2017

Detection of diffuse seafloor venting using a structured light laser sensor: 2. Evaluation of detection sensitivity and limitations

Clara Smart
University of Rhode Island

Chris Roman
University of Rhode Island

Citation/Publisher Attribution

Smart, Clara, and Chris Roman. "Detection of diffuse seafloor venting using a structured light laser sensor: 2. Evaluation of detection sensitivity and limitations." *Earth and Space Science* 4, 6 (2017): 364-376. doi: 10.1002/2017EA000263.

Detection of diffuse seafloor venting using a structured light laser sensor: 2. Evaluation of detection sensitivity and limitations

Keywords

hydrothermal vent detection; hydrothermal venting; mapping; remote imaging; structured light laser sensor; system limitations

AGU PUBLICATIONS

Earth and Space Science

RESEARCH ARTICLE
10.1002/2017EA000263

This article is a companion to *Smart et al.* [2017], doi:10.1002/2017EA000262.

Key Points:
- Impacts of survey parameters on the structured light laser vent detection algorithm are studied
- Normalization and processing algorithms which account for higher-altitude surveys are presented
- The spatial distribution of the detected density anomaly may indicate plume rise height

Correspondence to:
C. Smart,
csmart@my.uri.edu

Citation:
Smart, C., and C. Roman (2017), Detection of diffuse seafloor venting using a structured light laser sensor: 2. Evaluation of detection sensitivity and limitations, *Earth and Space Science*, *4*, 364–376, doi:10.1002/2017EA000263.

Received 7 FEB 2017
Accepted 17 MAY 2017
Accepted article online 9 JUN 2017
Published online 28 JUN 2017

Detection of diffuse seafloor venting using a structured light laser sensor: 2. Evaluation of detection sensitivity and limitations

Clara Smart[1] **and Chris Roman**[1,2]

[1]Department of Ocean Engineering, University of Rhode Island, Narragansett, Rhode Island, USA, [2]Graduate School of Oceanography, University of Rhode Island, Narragansett, Rhode Island, USA

Abstract Algorithms to detect diffuse hydrothermal vent fluids using the structured light laser sensor have proven to be successful. However, potential limitations due to survey parameters, including altitude and vehicle heading, have not been explored and are the focus of this study. Data from 12 surveys conducted over a single hydrothermal vent at three different altitudes (2.7 m, 4.2 m, and 6.2 m) and four different headings are analyzed. Increasing survey altitude decreases the resolution and intensity of the imaged laser line; therefore, range-dependent processing considerations to maintain detection sensitivity are presented. Analysis of these surveys suggests minimal degradation of vent detection capabilities from survey altitudes up to 6 m. Additionally, as the shape and location of the detected distortion patterns vary with survey heading and altitude they are presented as potential indications of plume shape and rise height. The effects of range and survey heading are important for future applications of this sensor which may include surveying from higher, faster flying autonomous underwater vehicles.

1. Introduction

1.1. Justification for Study

Algorithms for detecting turbulent fluid anomalies associated with diffuse hydrothermal activity using a structured light laser sensor have been previously developed [*Smart et al.*, 2013, 2017]. Distortion of a projected laser line due to interaction with fluid density anomalies can be detected using image processing techniques. The resulting data allow for the creation of maps indicating the spatial distribution of areas of active fluid flow. A typical vehicle survey altitude for optical imaging is 3 m, and while range variations on the order of a meter occur within and between surveys, the implications of surveying at higher altitudes have not been considered. The impacts of range and light attenuation on signal quality and vent detection capabilities are the focus of this study.

Currently, the structured light laser sensor and stereo cameras are optical imaging components of a high-resolution remotely operated vehicle (ROV) imaging system (Figure 1). Using the ROV's closed loop control system and suite of navigation sensors, it is possible to survey at a consistent altitude and velocity in an organized pattern [*Roman et al.*, 2012]. Future applications for the structured light laser sensor include integration into higher, faster flying autonomous underwater vehicles, which complete high-resolution bathymetric surveys from altitudes of 8 to 15 m [*German et al.*, 2008; *Yoerger et al.*, 2007]. Therefore, establishing the laser vent detection limitations due to altitude, speed, and other survey parameters will inform future design considerations and scientific applications.

1.2. Structured Light Laser Sensor

The structured light laser sensor consists of a 12 bit 1360 × 1024 pixel mono Prosilica GC1380 camera with a 30° by 40° field of view which images a 100 mW, 532 nm Coherent PowerLine sheet laser projected at an angle on the seafloor. The vertical position of the laser line within each image capture is proportional to range and can be converted to a single bathymetric profile, analogous to a single ping of range data from a multibeam sonar [*Inglis et al.*, 2012]. Additionally, the combination of the intensity and spread of the laser line allows for the detection of diffuse hydrothermal venting (as detailed in the companion paper Detection of diffuse hydrothermal flow using a structured light laser sensor: 1. Development of a classification based detection method [*Smart et al.*, 2017]). Typically, the vehicle travels at approximately 0.2 m/s as the laser line is imaged

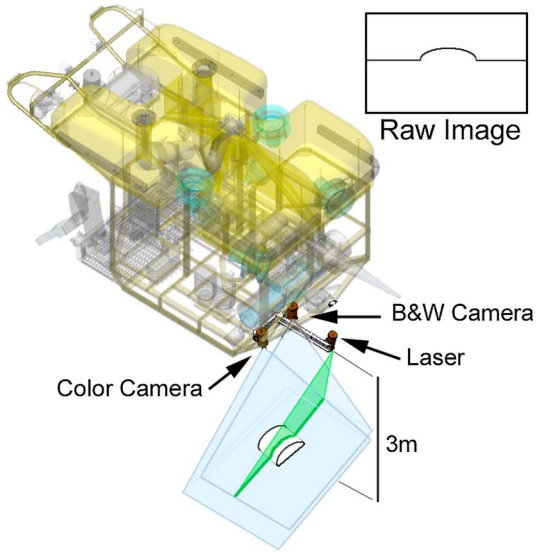

Figure 1. A computer rendering of ROV *Hercules* showing the stereo camera pair and structured light laser sensor mounted on the back of the vehicle away from operational lights. The projected sheet laser is imaged at the seafloor (inset).

from an altitude of 3 m at approximately 20 Hz, creating a survey resolution better than one laser line per centimeter along track and 2–4 points (pixels) per centimeter across track, with an associated range resolution of 0.5 cm per camera pixel.

1.3. Laser Line Interaction With Fluid Density Anomalies

The position and intensity of the laser line is determined from raw 12 bit black and white images which capture the laser line incident with the seafloor [*Inglis et al.*, 2012]. As the structured light sensor passes over active hydrothermal fluids the associated turbulent fluid density anomalies cause the laser light to scatter along the optical path and appear blurred, instead of crisp, within the captured image (Figure 2a). An insightful computation for establishing the spread of the laser line, which serves as a proxy for active venting, is the unitless intensity-weighted second moment about the peak intensity value of the laser line, the extracted points depicted in Figure 2b, and is further detailed in *Smart et al.* [2017].

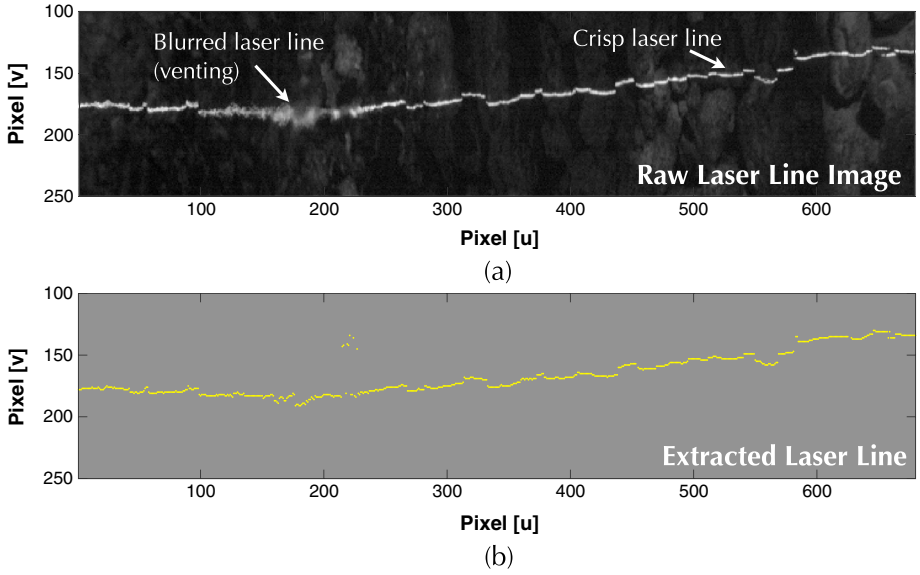

Figure 2. Laser line acquisition and extraction example. (a) A raw laser line image. In the presence of active venting the laser line becomes blurred instead of crisp. (b) The extracted laser line points correspond to the peak columnwise intensity.

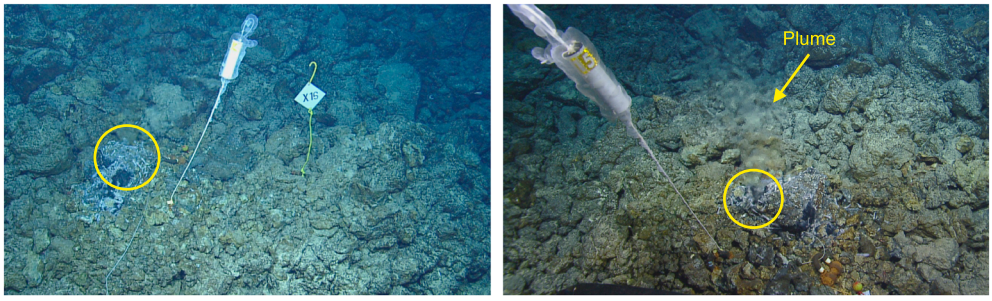

(a) (b)

Figure 3. Images of the vent site acquired with the ROV mounted HD video cameras, the vent orifice is circled. (a) The vent orifice surrounded by rocky seafloor with both markers are visible. (b) The blur in the center of the photo indicates a rising plume.

2. Site Overview and Data Acquisition

The approximately 110 km long Mid-Cayman Spreading Center in the Caribbean Sea is one of the worlds deepest ultra slow spreading centers. The isolated small hydrothermal vent presented in this study is located within the Von Damm Vent field, at a depth of 2300 m along the upper slopes of the Mount Dent Oceanic Core Complex [*Connelly et al.*, 2012]. This site was previously visited with ROV *Jason* during the 2012 OASES Research Cruise and by DSV *Shinkai 6500* during the 2013 YK13-05 cruise. Remaining scientific markers, floating a meter above the seafloor, include a metal diamond-shaped marker labeled "X-16" and a second white tube-like marker labeled "154" both placed near the vent orifice (Figure 3a) [*Independent Administrative Institution, Japan Agency for Marine-Earth Science and Technology, Yokosuka, Japan*, 2013].

Exploration of the vent site on 21 August 2013 using the ROV *Hercules*, operating from E/V *Nautilus*, included collecting high-definition video footage and temperature data. A small but visible plume was observed rising a meter above the rocky seafloor and is visible as blur in the center of Figure 3b. Clear, focused flow emanated from an approximately 10 cm wide vent orifice, circled, around which small shrimps are present. Collected temperature probe data indicated that ambient seawater was 4.25°C and the maximum temperature of the venting fluids was 29.52°C. The surrounding area contained minimal bacterial mat coverage, a few shrimp, many dead mussel shells, and scientific markers.

2.1. High-Resolution Imaging Survey

To determine the impact of altitude and sensor orientation on vent detection results, a series of survey grids with varying altitudes and vehicle headings were completed over an approximately 15 m × 15 m area around the single hydrothermal vent. A comprehensive view of the rocky site is presented in the color photomosiac (Figure 4a) with the small vent orifice circled. The resulting structured light vent detection map in Figure 4b illustrates sensitivity to diffuse hydrothermal venting. Surveys collected 2.7 m, 4.2 m, and 6.2 m above the seafloor are identified as the 2 m, 4 m, and 6 m surveys, respectively. The vent orifice was passed over at four different vehicle headings, 75°, 165°, 255°, and 345°, at each altitude, resulting in 12 individual surveys of the area. The resulting vehicle navigation for each altitude is shown in Figure 5. Mapping was completed within 2.5 h.

ROV *Hercules* is closed loop controlled and capable of executing track lines at prescribed velocities, altitudes, and depths. The navigation sensor suite includes a 600 kHz RDI Doppler Velocity Log (DVL), IXSEA OCTANS fiber-optic gyroscope, and a Paroscientific depth sensor [*Bell et al.*, 2016]. These data are collected using the DVLNAV software package [*Kinsey and Whitcomb*, 2004].

3. Impact of Range on Geometry

The structured light laser system is mounted on a rigid frame and calibrated by establishing the laser plane by triangulating stereo features along the laser line as outlined in [*Inglis et al.*, 2012]. No adjustments are made to the laser angle or system geometry for changes in survey altitude. Specifically, the sheet laser has a 40° field of view and is mounted at an 11.7° angle allowing the sheet laser to intersect the center of the 30° × 40° field of view of the mono 1024 × 1360 pixel camera from an altitude of 3 m. To maximize laser frame rate during acquisition, the laser images are horizontally downsampled to 680 pixels and cropped vertically. The laser

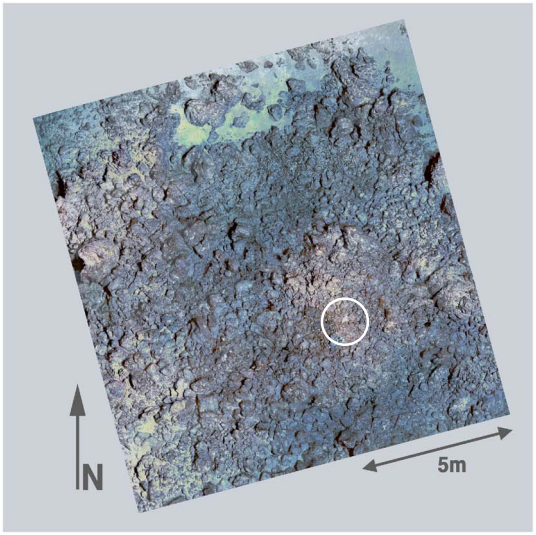

(a)

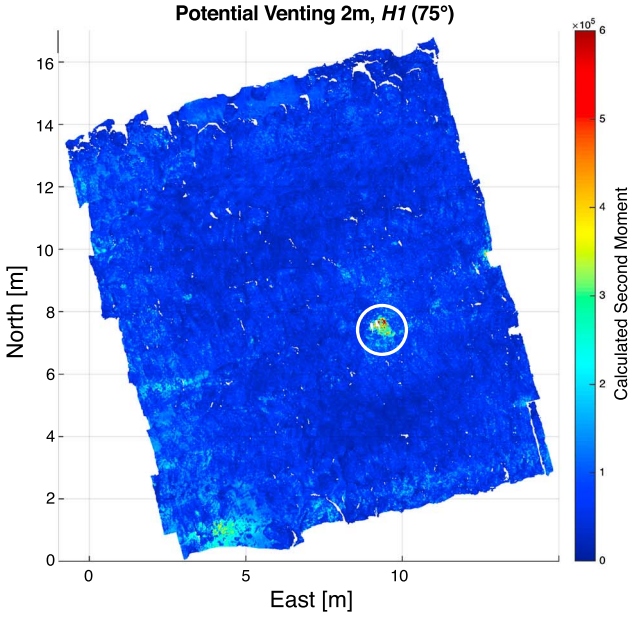

(b)

Figure 4. High-resolution imaging results show a rocky area with mussel shells, minimal biology, and scientific markers. (a) Photomosaic composed of 300 images shows a barely distinguishable small hydrothermal vent, circled. (b) Gridded vent detection results from 2 m data indicate active venting, circled, in the southeast quadrant.

line field of view, projection distance, and along-track range will increase with vehicle altitude, while resolution will decrease. Projection distance is defined as the laser raypath distance between the laser source and seafloor and is slightly greater than the vehicle altitude as the laser is verged. Table 1 summarizes resolution and geometric changes based on altitude.

4. Impact of Range on Detection

4.1. Attenuation in Seawater

Attenuation of light in seawater is dependent on range and absorption. Range is determined by the vehicle altitude and includes both the raypath distance from the laser to the seafloor and the return path to the camera, making the attenuation distance roughly twice the survey altitude. The attenuation coefficient is dependent on the wavelength of the laser, water chemistry, and particulates within the water column. As true

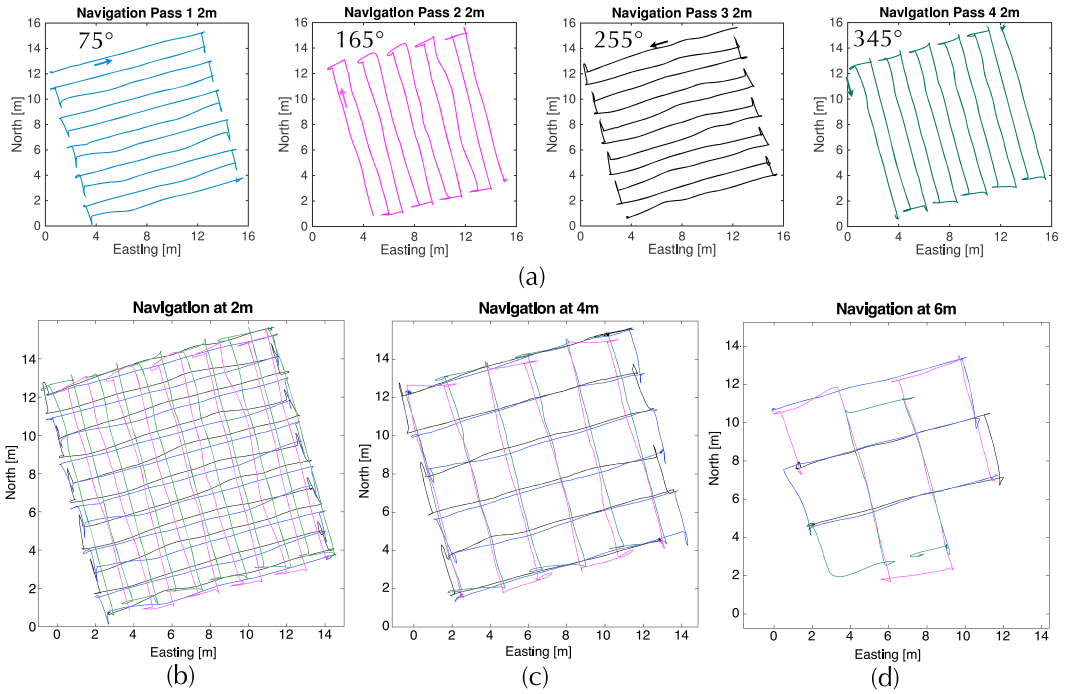

Figure 5. Navigation corresponding to three surveys at nominal altitudes of 2.7 m, 4.2 m, and 6.2 m surveyed from four headings. (a) Navigation corresponding to surveys completed from 2.7 m with the vehicle headings set to (from left to right) 75°, 165°, 255°, and 345°. Combined navigation for (b) 2.7 m, (c) 4.2 m, and (d) 6.2 m surveys.

scattering values are unknown for this site, the diffuse attenuation coefficient for "irradiance of clearest ocean waters" of 0.0519 m^{-1} for ideal pure seawater at a wavelength of $\lambda = 530$ nm given in [*Smith and Baker*, 1981] will be used. The total loss due to attenuation can be calculated using Beer-Lambert's law

$$I_r = I_i \times e^{-kr}, \tag{1}$$

where I_i is the initial intensity of the light, $k = 0.0519$ m^{-1} is the attenuation coefficient, r is range, and I_r represents the resulting intensity. Initial computations indicate that at a survey altitude of 2.7 m $I_r = I_i \times 0.75$ while at 6.2 m $I_r = I_i \times 0.53$. The diffuse attenuation coefficient for pure seawater is a low estimate for this field site, and the actual losses are likely higher due to suspended particulates, chemical composition, and the turbulent flow.

4.2. Intensity Variations

Attenuation causes range and the imaged laser line intensity to be inversely proportional. Figure 6a shows the mean of 680 aligned laser line cross sections captured over an area without venting. Due to increased

Table 1. Geometric and Resolution Values Corresponding To Survey Altitudes Between 2 m and 6 m

	Field of View		Pixels per cm			
Altitude (m)	Vertical (m)	Horizontal (m)	Full Frame	Sampled Horizontally	Projection Distance (m)	Along Track Range Distance (m)
2.0	1.07	1.46	9.34	4.67	2.04	0.41
2.5	1.34	1.82	7.47	3.74	2.55	0.52
3.0	1.61	2.18	6.23	3.11	3.06	0.62
3.5	1.88	2.55	5.34	2.67	3.57	0.72
4.0	2.14	2.91	4.67	2.34	4.08	0.83
4.5	2.41	3.28	4.15	2.08	4.60	0.93
5.0	2.68	3.64	3.74	1.87	5.11	1.04
5.5	2.95	4.00	3.40	1.70	5.62	1.14
6.0	3.22	4.37	3.11	1.56	6.13	1.24

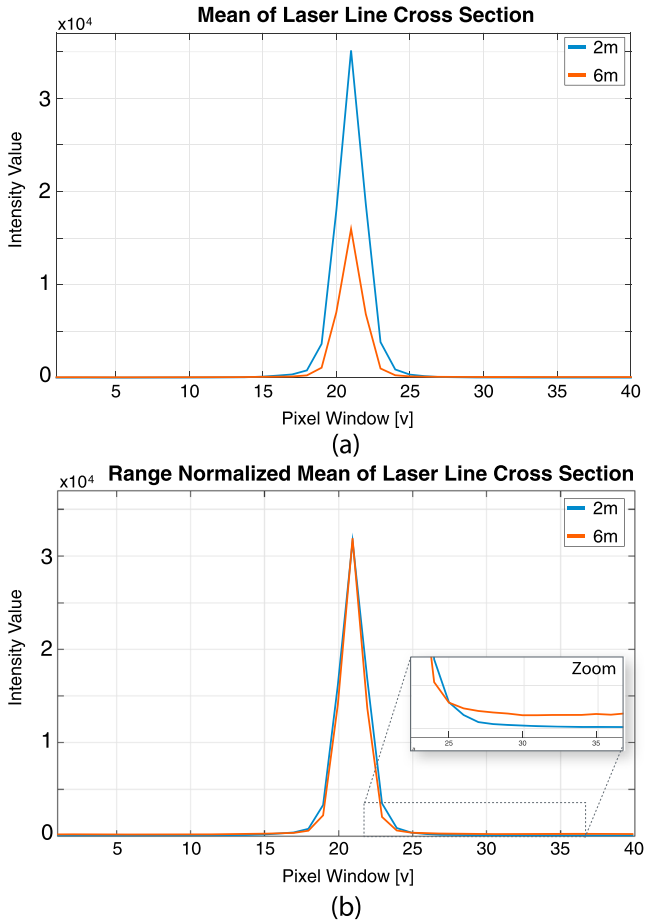

Figure 6. Mean of 680 laser line cross sections. (a) Without range normalization the 6 m laser line has an intensity approximately 55% lower than the 2 m data. (b) Range normalized intensities show that 2 m and 6 m values are nearly equivalent. Comparing the mean of the surrounding pixels indicates that the 6 m data have a noise floor which is only slightly higher than 2 m (inset).

attenuation, the 6 m peak intensity is approximately 55% lower than the 2 m peak. This difference is greater than the theoretical 30% decrease in intensity between the two survey altitudes, likely because the theoretical values are computed in ideal seawater, not an area of active hydrothermal activity.

Range-based intensity normalization includes multiplying the measured intensity by the ratio between the measured and desired range, effectively representing data as if it were collected from a single known altitude. Once normalized the presented intensity results are very similar (Figure 6b). This allows for direct comparison of intensity data collected from various altitudes.

4.3. Signal-to-Noise Ratio

Within a laser line image the desired signal is the laser line while noise is defined as the primarily black background. Despite the reduction in image intensity with increased range, the signal-to-noise ratio does not significantly degrade. This is illustrated by Figure 6b (inset) in which the mean of normalized background values, located on either the laser line peak, shows little deviation between the two altitudes. While noise levels increase with range the noise floor in both cases is less than 3% of the maximum of the normalized intensity. Therefore, the signal-to-noise ratio does not degrade notably up to a survey altitude of 6.2 m.

5. Processing Considerations

Detection of diffuse hydrothermal venting using the structured light laser sensor utilizes an intensity-weighted second moment to capture the blur associated with the fluid anomaly. This computation considers the intensity of each pixel within a specific window about the peak of the laser line. In the presence of active

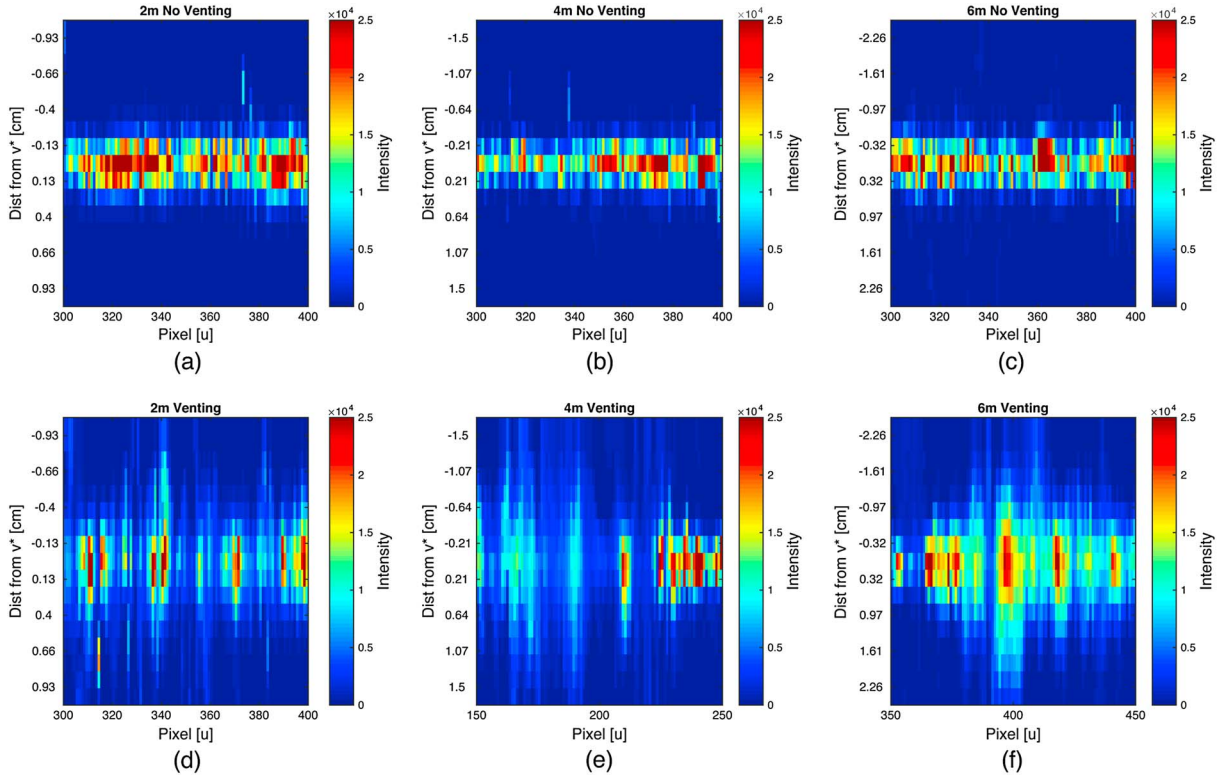

Figure 7. Aligned laser line cross sections illustrate the impact of range and the presence of venting on the laser intensity. (a–c) Data collected over areas without venting and shows a crisp laser line consistently 3 pixels wide, independent of range. (d–f) Data collected where anomalous fluid density interaction increases the laser line width.

venting, the width of the laser line increases, which is apparent in Figure 7 which depicts intensity values for 100 aligned laser line cross sections with and without venting collected from three altitudes. An undistorted crisp laser line over plain seafloor covers approximately 3 pixels, independent of range (Figures 7a–7c). However, 3 pixels equates to 0.26 cm in the 2 m case and 0.64 cm at 6 m. Pixel size relative to altitude is outlined in Table 1. As the laser line passes over fluid density anomalies the overall intensity tends to decrease while the width of the laser line increases (Figures 7d–7f). The associated blur can be observed at least a centimeter on either side of the laser line in all cases.

Establishing the correct window size for the second moment computation will impact vent detection results, which are presented as geospatial maps (Figure 8). As the window size decreases the computation becomes sensitive to intensity variations within the data, creating false positives. Conversely, if a window is too large, excessive background pixels cause a lack of sensitivity resulting in a loss of detail. Figure 8 illustrates the impact of window size on the second moment computations, for data collected at an altitude of 4 m. A 1.2 cm (7 pixels) window about the laser line peak is shown in Figure 8a. This window is too small and is sensitive to slight fluctuations in the intensity of the laser line as indicated by the many bright spots within this image. Although these elements could be caused by fluid anomalies, the prevalence and distribution imply that they are the results of changes in seafloor intensity or other scattering within the water column. Conversely, a 3.5 cm (17 pixels) window shown in Figure 8c is large enough to include background seafloor variations not illuminated by the laser line. This can be further understood by looking at the 4 m laser line cross sections shown in Figure 7. A window which is too large emphasizes seafloor characteristics, as observed by the detected spot along the northern edge of the survey and the horizontal artifact in the center of the survey. A balance between a window large enough to accommodate the increased laser line width in the presence of active venting but small enough to limit the role of nonilluminated background pixels is necessary. In this case a window 2 cm wide (11 pixels) about the laser line peak (Figure 8b) was determined experimentally. While completely eliminating artifacts is not possible, matching the computation window size with the amount of laser line spread and evaluating resulting data for systematic imaging and seafloor artifacts improve detection accuracy.

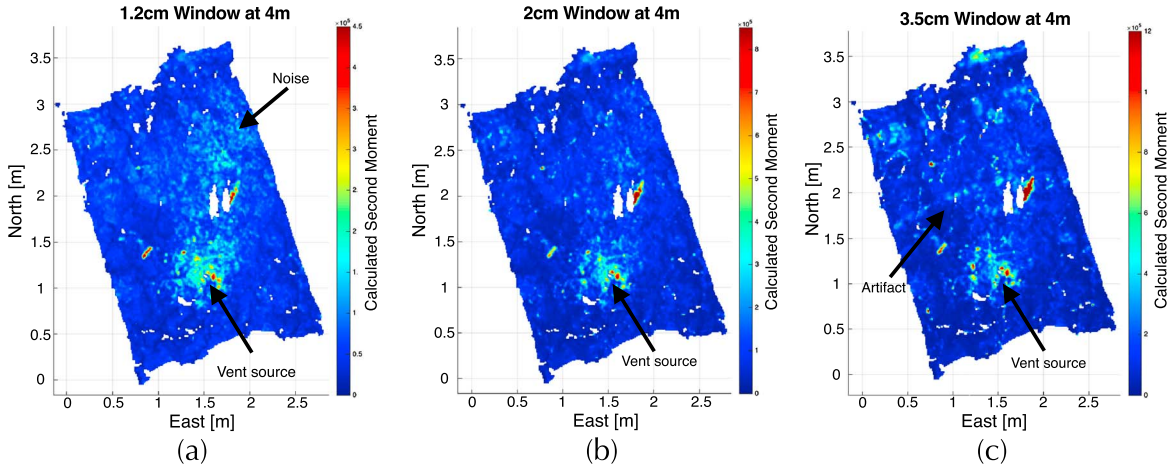

Figure 8. Gridded survey results comparing different windows for the second moment computation. (a) 1.2 cm (7 pixels) window about the laser line peak allows for slight anomalies to dominate, creating a noisy image. (b) 2 cm (11 pixels) window allows for clear detection of the fluid anomaly. (c) 3.5 cm (17 pixels) window is too large and allows background pixels to influence the computation.

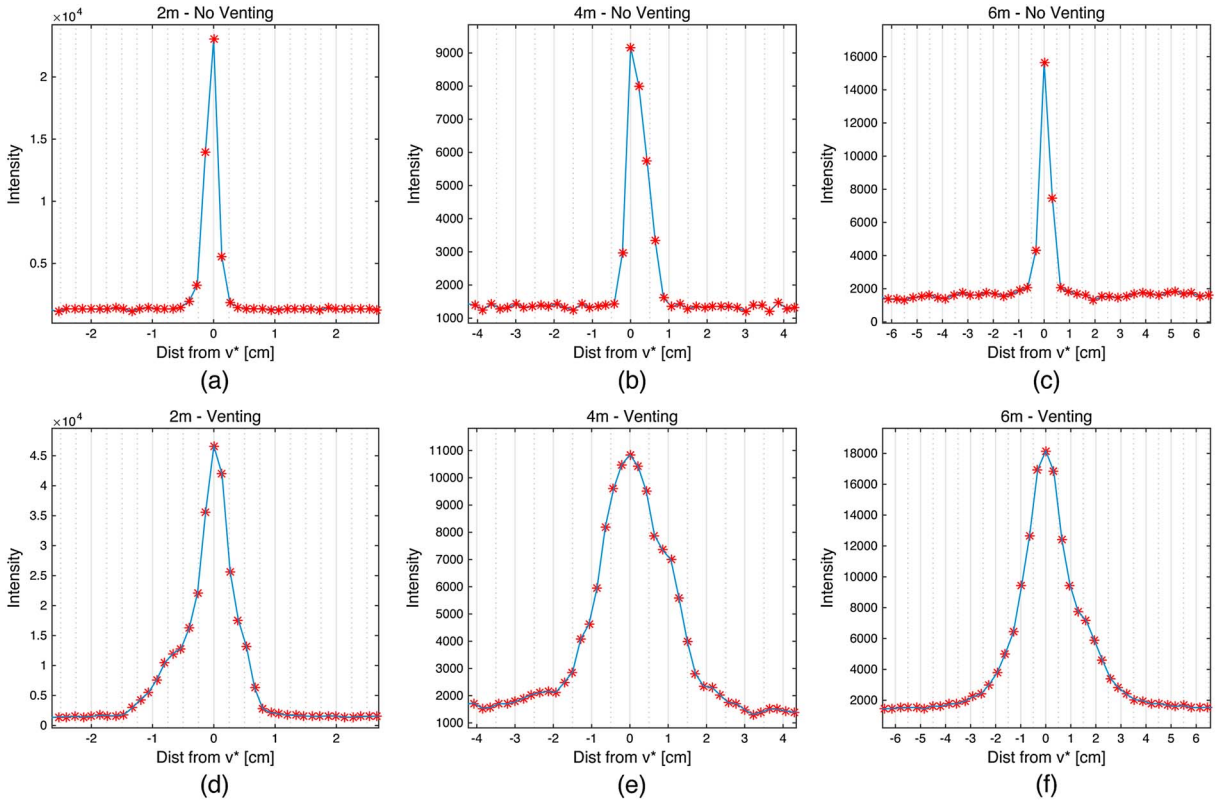

Figure 9. Comparisons of laser line cross sections illustrate the size of the second moment computation window for each altitude. Each cross section includes 20 pixels, represented by red asterisks, on each side of the peak intensity, v^*. The x axis corresponds to the seafloor distance from the peak of the laser line in centimeters. Cross sections depicted in Figures 9a–9c correspond to data collected over an area without venting, while the laser line in Figures 9d–9f is distorted due to active venting. (a and d) 2 m data with approximately 7.5 pixels/cm. (b and e) 4 m data with 4.7 pixels/cm. (c and f) 6 m data which has the lowest resolution with 3 pixels/cm.

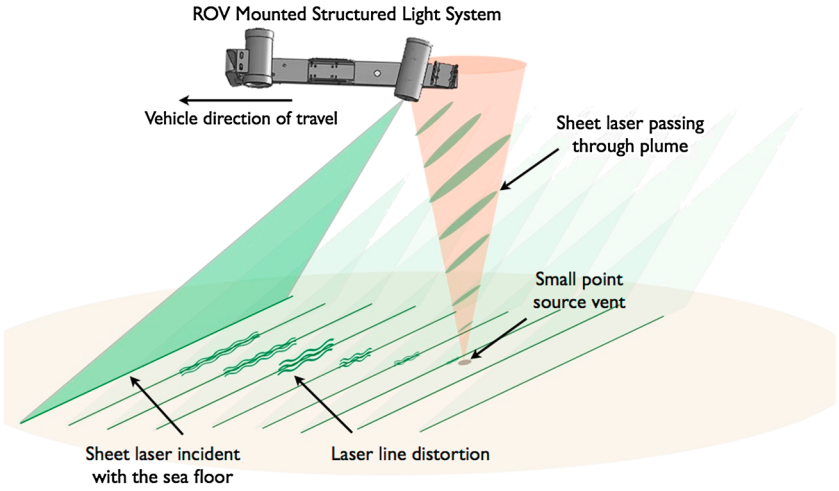

Figure 10. While surveying active vent sites, the sheet laser passes through active turbulent flow of varying index of refraction values resulting in a blurred and distorted laser line projected on the seafloor.

Vent detection results which are consistent between surveys require a second moment computation window of a constant width; therefore, the number of pixels within the window must change with survey altitude. Figure 9 shows laser line cross sections containing 40 pixels (red asterisks) for each altitude at the same non-venting and venting locations. The *x* axis denotes centimeters from the center of the laser line. Over plain seafloor it is notable that the width of the laser line is consistent, just under 0.5 cm to either side of the laser line peak and is independent of range. Over active venting the width of the laser line varies more, for example, the laser line pixels in the 2 m case will be mostly found within 1.25 cm of the peak of the laser line while this distance increases to 2.5 cm in the 6 m case. However, over active venting the majority of the laser line blur is contained within approximately 1 cm from the laser line peak, effectively defining computational window, which is consistent with the previously established results and Figure 8b. The number of pixels which make up this window varies with range, approximately 17 pixels at 2 m, 11 pixels at 4 m, and 7 pixels at 6 m. Implementing the second moment window-dependent range, instead of a fixed number of pixels, will produce vent detection results comparable between different survey altitudes.

6. Detection of Disturbances

Ideally, the geometry of the observed scattering will indicate the distribution and rise height of the anomalous fluid. Interactions between the sheet laser and anomalous fluid meters above the seafloor will be projected beyond the vent, as a function of the laser sheet angle. As the vehicle travels past a vent the observed blur will continue until the fluid anomaly no longer intersects the laser plane (Figure 10). For instance, as a sheet laser passes through an ideal cylindrical volume of fluid rising into the water column a triangular distortion pattern will be projected onto the seafloor, proportionally increasing in width with the distance between the vent orifice and projected laser line. The along-track laser projection varies with altitude, as does the seafloor area under the sheet laser (Table 1). Conversely, diffuse flow pooling at the seafloor will be intersected by the sheet laser at or near the seafloor and the associated distortion pattern will appear less defined, corresponding in shape to spatial distribution of fluid, which should not be heading dependent. Surveying a fluid anomaly from multiple headings will establish the plume shape characteristics perpendicular to each heading, ideally, providing insight into the three-dimensional structure of a rising plume.

Four passes labeled *Heading 1–4 (H1–4)*, at each altitude, have been completed (Figure 5) and will be used to compare differences in plume detection and shape. A mosaic of mono images acquired over the active vent site showing blur associated with fluid flow and the scientific markers is shown in Figure 11. Comparisons between surveys will be made based on segments of approximately 200 laser lines covering the area of active venting (Figures 12–14). Within the laser images occlusions due to the markers are visible as holes in the data. The association between the laser line swath width and altitude is apparent as the survey patch width increases for higher altitudes.

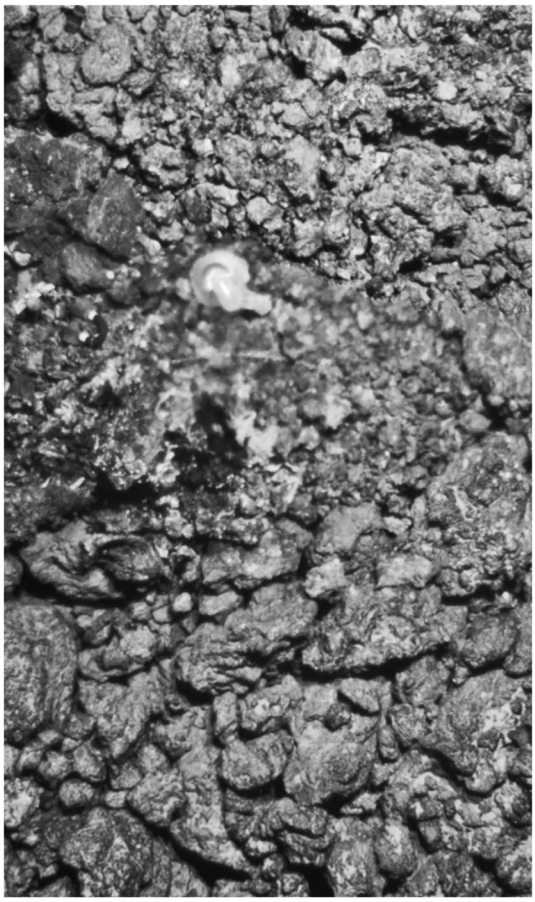

Figure 11. A mosaic image acquired by the mono camera during the 4 m survey in which blur due to active venting of hydrothermal fluids and markers is present.

6.1. Distribution of Laser Line Distortions

Due to the forward angle of the projected laser sheet, the majority of the distortion appears on the opposite side of the vent orifice. For each heading the area of laser line distortion has been simplified to an ellipse. The four ellipses representing the projected laser line distortion are displayed on the same plot within Figures 12–14. Within these figures navigation error (further discussed in section 6.3) has been accounted for, allowing each heading and altitude to appear on the same axes.

In the ideal scenario, depicted in Figure 10, the four ellipses would be arranged relative to the survey heading and overlap at the vent orifice. Within the presented data, elements of this expected behavior are present, although inconsistent. For instance, within the 2 m diagram (Figure 12) the alignment between *H1* and *H3* correlates to a plume rising into the water column from an orifice located within the shared distortion area, for instance at $x = 2.25$ and $y = 3.25$. However, the *H2* and *H4* areas of distortion almost overlap entirely along the direction of travel, indicating less rise height. These four ellipses share a common area of approximately 0.125 m^2, which correlates to the location of the vent orifice.

Within the 4 m results the distortion map is less coherent as the ellipse corresponding to *H1* is separated from the others (Figure 13). Despite this, the alignment between *H1* and *H3* is logical. Additionally, the lateral adjacency of *H2* and *H4* does not indicate a plume rising vertically into the water column, rather possibly east-west advection. Due to the offset nature of *H1*, there is no common distortion area within this figure; however, the remaining three distortion ellipses share a small common area about $x = 2.75$ and $y = 3.25$, which is consistent with the 2 m data. Furthermore, the tight cluster of ellipses within the 6 m data indicates a shared area of fluid anomalies but hardly resembles the ideal case projection (Figure 14). Projections for *H1* and *H3* share the same area, while *H2* and *H4* overlap, offset to the south. Temporal variability may also account for observed differences between the 2 m and 6 m data.

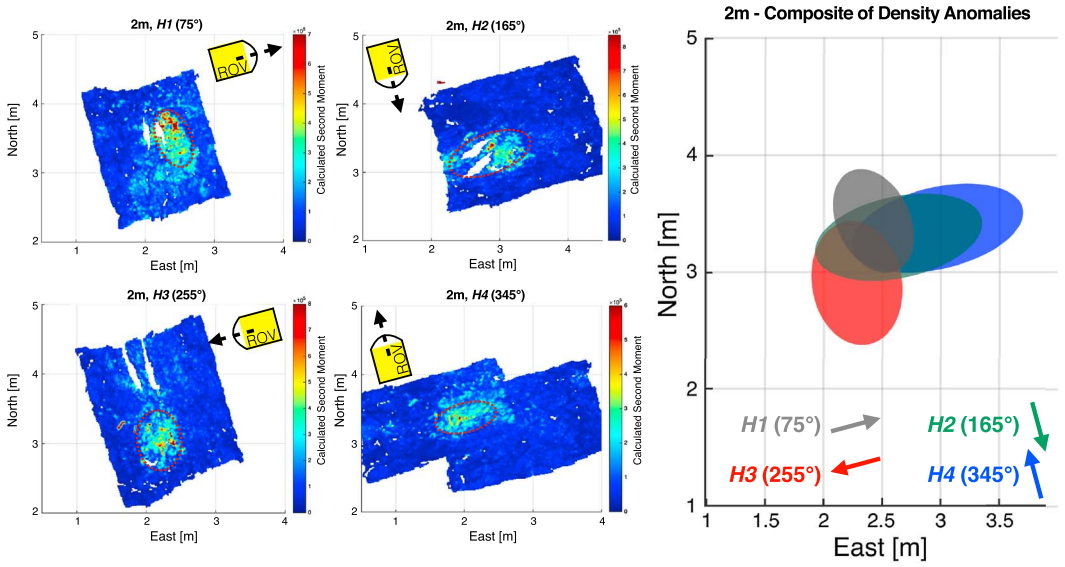

Figure 12. Comparison of navigation-corrected vent detection results collected at 2 m from headings *H1–4*. Each distortion pattern has been simplified to an ellipse to clarify the extent and location. The observed distortion for *H4* was split between adjacent overlapping survey lines.

6.2. Geometric Changes Due To Range

While the across-track width of the detected vent anomaly should be comparable for surveys of reciprocal headings, the along-track distortion should increase with altitude. Once beyond the vent, anomalous fluids no longer interact with the sheet laser, as apparent to the east of the anomaly in the 2 m *H1* pass (Figure 12). Within the presented results, the *H1* and *H3* headings show an across-track distortion width between 0.5 m and 0.75 m, while the along-track distortion distance varies between approximately 0.5 m at 2 m altitude and 1 m for 6 m altitude (*H1*). Considering the projection distance of the sheet laser, the observed along-track distortion can be used to estimate rise height using Table 1; this assumes distortion caused only by rising fluids. For instance, in the 2 m case the 0.5 m along-track distortion range correlates to a detection altitude

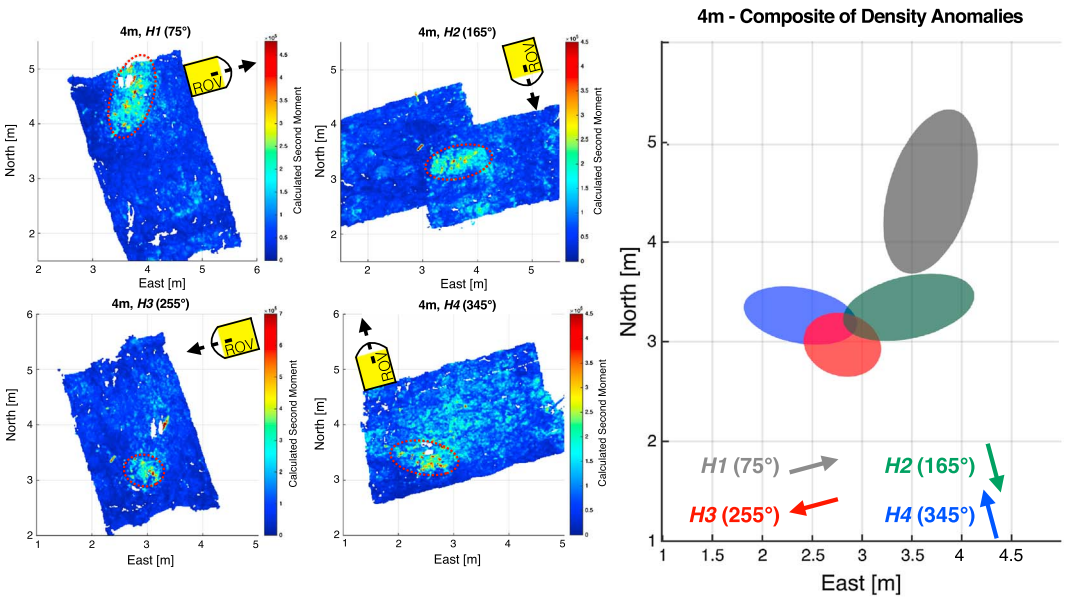

Figure 13. Comparison of navigation-corrected vent detection results collected at 4 m from headings *H1–4*. Each distortion pattern has been simplified to an ellipse to clarify the extent and location. The observed distortion for *H2* was split between adjacent overlapping survey lines.

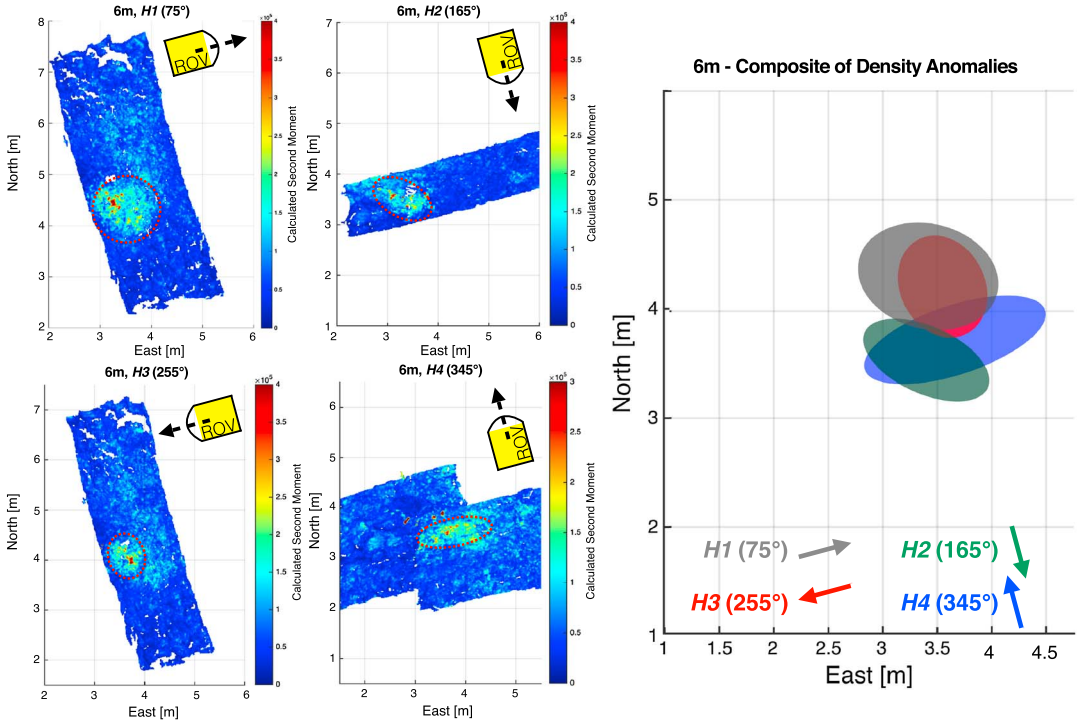

Figure 14. Comparison of navigation-corrected vent detection results collected at 6 m from headings *H1–4*. Each distortion pattern has been simplified to an ellipse to clarify the extent and location. The observed distortion for *H2* was split between adjacent overlapping survey lines.

of 2.5 m, effectively at the vehicle. Additionally, the 1 m along-track distortion observed in the 6 m data indicates that the fluid is detected rising 5 m above the seafloor.

Distortions observed within the *H2* and *H4* data are larger in the across-track dimensions, consistently 0.5 m along track and 1–1.5 m across track, independent of altitude. This ratio may imply that the plume does not rise to 5 m as previously noted but rather spreads in the direction of vehicle travel. Considering that the distortion is detected 0.5 m laterally from the vent orifice, from this perspective the plume could be rising a maximum of 2.5 m. A combination of rise height and lateral diffusion would explain the observed differences between survey altitudes.

6.3. Navigation Error

The primary navigation sensor used during the survey process is a Doppler Velocity Log (DVL) which determines current position based on the previous position and integrated velocity vectors. Over time cumulative error can result in navigation values which have drifted on the order of tens of centimeters. As a result, a specific feature on the seafloor does not have identical *X-Y* locations within each survey. DVL drift is corrected by resetting DVL to a position determined by the Ultra Short Baseline (USBL) sensor system which includes transponders mounted on the ship and the ROV. However, reinitializing the location of the DVL was not done during the survey to prevent navigation discontinuity as error associated with this USBL system is up to 5% of water depth.

To counter the navigation error and present coregistered data, the location of a specific feature on the seafloor will serve as a navigation reference point. The shackle with reflective tape which is located to the left of the plume (Figure 11) was identified within the coregistered stereo images acquired during the 2 m and 4 m surveys. Stereo images were not collected during the 6 m survey due to altitude; however, this shackle was located within collected laser intensity data. When available, preference was given to the stereo images due to the increased resolution. Variance in shackle location was subsequently treated as a navigation offset allowing for the correction of survey positions.

7. Further Study

Given the robust laser line signal at 6 m altitude, signal limitations should be tested and established at even higher survey altitudes. Eventually, due to attenuation and scattering, the laser will become too faint to detect. Additionally, the potential for nonvent-related disturbances to the sheet laser due to water quality and biological activity will increase with range.

Survey limitations to consider at higher altitudes are the laser power and camera parameters. The current sensor suite is optimized to operate at an altitude of 3 m; therefore, the laser is low power (100 mW) and a standard 12 bit computer vision camera is used. Increasing the power of the laser and using a camera better suited for low light applications will increase the laser line detection at increased survey altitudes. Additionally, increasing the resolution of the camera will allow for comparable resolution within the laser line captures.

The vent site studied within this paper included a relatively low fluid flux, low temperature focused flow vent site with a plume which was not visibly detected more than a meter above the seafloor. Surveying a larger focused flow vent would provide additional insight into the possibility of determining rise height and the behavior of the plume using the pattern of the laser line on the seafloor as outlined in section 6 and shown in Figure 10. Although slightly tedious, the multiple survey orientations and altitudes demonstrate the potential to glean information about the disturbance in the water column. This is encouraging, as understanding rise height, and therefore, plume buoyancy may lend itself to further quantification of volume or heat flux rates. High-quality navigation will further establish the location of the vent orifice and three-dimensional structure.

8. Conclusion

Varying survey altitudes alter the resolution and intensity of the imaged laser line but does not obscure detection of fluid anomalies if processing parameters are adjusted to account for changes in range. The direction of the sheet lasers projection can indicate the structure of a hydrothermal plume or the distribution of fluid anomalies within the water column. The presented detection and signal-to-noise results are promising considering the aim of operating this sensor at higher altitudes from an autonomous underwater vehicle as a part of general site mapping.

Acknowledgments
The authors would like to acknowledge support of the Roman Lab at the University of Rhode Island and the Ocean Exploration Trust which operates the E/V *Nautilus*. Data collection was completed using ROV *Hercules*, owned and operated by Ocean Exploration Trust. Expedition data, including vehicle sensor data, navigation data, video footage, and HD imagery, are available through Ocean Exploration Trust (http://www.oet.org/data-request). High-resolution survey data, including stereo images and structured light laser captures, are available through Chris Roman, Graduate School of Oceanography, University of Rhode Island (croman2-at-uri-dot-edu).

References

Bell, K. C., M. L. Brennan, J. Flanders, N. Raineault, and K. Wagner (2016), Technology, exploration vessel Nautilus, *Oceanography*, *29*(1), 4–9, doi:10.5670/oceanog.2016.supplement.01.

Connelly, D. P., et al. (2012), Hydrothermal vent fields and chemosynthetic biota on the world's deepest seafloor spreading centre, *Nat. Commun.*, *3*, 620.

German, C. R., D. R. Yoerger, M. Jakuba, T. M. Shank, C. H. Langmuir, and K. Nakamura (2008), Hydrothermal exploration with the autonomous benthic explorer, *Deep Sea Res., Part I*, *55*(2), 203–219.

Inglis, G., C. Smart, J. Vaughn, and C. Roman (2012), A pipeline for structured light bathymetric mapping, paper presented IEEE/RSJ International Conference on Intelligent Robots and Systems, Vilamoura, Algarve, Portugal, 7–12 Oct.

JAMSTEC (2013), R/V Yokosuka and DSV Shinkai 6500 cruise report yk13-05: Geochemical, geomicrobiological and biogeographical investigation of deep-sea hydrothermal activities in the Mid Cayman Ridge, the Caribbean, Cruise Rep., Japan Agency for Marine-Earth Science and Technology (JAMSTEC), Yokosuka, Japan.

Kinsey, J. C., and L. L. Whitcomb (2004), Preliminary field experience with the DVLNAV integrated navigation system for oceanographic submersibles, *Control Eng. Pract.*, *12*, 1541–1549.

Roman, C., G. Inglis, J. I. Vaughn, C. Smart, B. Douillard, and S. Williams (2012), The development of high-resolution seafloor mapping techniques, *Oceanography*, *25*(1), 42–45.

Smart, C., C. Roman, and S. Carey (2017), Detection of diffuse seafloor venting using a structured light laser sensor: 1. Development of a classification based detection method, *Earth Space Sci.*, *4*, doi:10.1002/2017EA000262, in press.

Smart, C. J., C. Roman, and S. N. Carey (2013), Detection of diffuse seafloor venting using structured light imaging, *Geochem. Geophys. Geosyst.*, *14*, 4743–4757, doi:10.1002/ggge.20280.

Smith, R. C., and K. S. Baker (1981), Optical properties of the clearest natural waters (200–800 nm), *Appl. Opt.*, *20*(2), 177–184.

Yoerger, D. R., A. M. Bradley, M. V. Jakuba, C. R. German, T. M. Shank, and M. A. Tivey (2007), Autonomous and remotely operated vehicle technology for hydrothermal vent discovery, exploration, and sampling, *Oceanography*, *20*(1), 152–161.